PCCP

ROYAL SOCIETY OF CHEMISTRY

PAPER

View Article Online
View Journal

Cite this: DOI: 10.1039/d4cp04277h

Investigations of the structural, electronic, and optical properties of Ti_3XC_2 (X = Ge, Pb, or Bi) by DFT

Haider Hussain, *[a] Zulfiqar Ali Shah,[a] Syed Zafar Ilyas,[a] Abdul Shakoor *[b] and Zawar Hussain[ac]

Received 9th November 2024,
Accepted 3rd February 2025

DOI: 10.1039/d4cp04277h

rsc.li/pccp

The global community currently faces significant challenges in meeting the rising demand for energy production. The development of clean energy technologies has gained substantial attention due to increasing energy shortages and worsening environmental degradation. Addressing these challenges requires the development of new materials. This study investigates the structural, electronic, and optical properties of Ti_3XC_2 (X = Ge, Pb, or Bi) MXenes, focusing on deintercalation and intercalation stages. The structural analysis demonstrates that the insertion and removal of Ge, Pb, and Bi within Ti_3XC_2 MXene significantly affect cell volume, with the second deintercalation stage exhibiting greater structural stability compared to the first. These MXenes exhibit metallic conductivity confirmed by density of states (DOS) calculations which reveal a zero band gap even with GGA corrections. The optical properties, including reflectivity, dielectric function and energy loss highlight distinct behavior among the intercalated structures, particularly for **Ti_3GeC_2** which shows higher energy loss peaks in the 14–16 eV range. These findings provide valuable insights into the electronics and structural behavior of Ti_3XC_2 MXenes, making them promising candidates for advanced energy storage and electronic applications.

1 Introduction

The increasing need for energy storage devices due to higher penetration of renewable energy resources, emphasizes the requirement for batteries that offer high performance and also have environmental benefits and lower production cost. Historically, transition metals like cobalt and nickel have been extensively employed in a range of energy storage devices, including portable lithium-ion batteries and large-scale redox flow batteries, such as those utilizing vanadium. To advance sustainable battery chemistry, current research is concentrated on substituting transition metal-based energy storage materials with graphene and MXenes. These alternatives are composed of earth-abundant elements like carbon, nitrogen, oxygen, and sulfur, which are more readily available and do not necessitate energy-intensive production processes.

Two-dimensional (2D) materials have gained considerable interest in the field of energy storage due to their atomic or molecular thickness, extended lateral dimension, and high aspect ratio. These properties enable the formation of short ion diffusion paths, a large specific surface area (SSA), and a substantial number of active sites, which collectively enhance rapid charge storage. Graphene exhibits a substantial theoretical SSA (2630 $m^2 g^{-1}$) and high conductivity ($\approx$35 100 S m^{-1}) and has been extensively studied for electric double-layer capacitors (EDLCs).[1–3] Although activated graphene electrodes possess a higher capacitance value (200–350 F cm^{-2}) than activated porous carbons (60–100 F cm^{-2}), the capacitance of graphene is still lower than that of redox materials. Other two-dimensional (2D) materials,[4] including transition metal oxides (TMOs, such as V_2O_5), transition metal dichalcogenides (TMDs, like MoS_2), layered double hydroxides (LDHs, such as Ni_2Co), phosphorene (*e.g.*, black phosphoren), and MXenes (*e.g.*, titanium carbide Ti_3XC_2), have also been investigated. Among these, TMOs, TMDs, LDHs, and phosphorene exhibit high theoretical capacities when used in pseudo-capacitors or batteries. However, their application is significantly constrained by poor electrical conductivity and cycling instability.[5–9] MXenes offer superior charge cycle stability and enhanced electrical conductivity.

MXenes represent a class of two-dimensional materials that have attracted substantial interest in the domains of supercapacitors[10] and batteries over the past decade. These materials

[a] *Department of Physics, Allama Iqbal Open University (AIOU), Islamabad, Pakistan. E-mail: 000002659@student.aiou.edu.pk, zulfiqar.shah@aiou.edu.pk, szilyas@hotmail.com, Zawar66@gmail.com*
[b] *Department of Electrical Engineering, NUST College of EME, Islamabad, Pakistan. E-mail: abdulshakoor@ceme.nust.edu.pk*
[c] *Ministry of Science and Technology, Islamabad, Pakistan. E-mail: jea@most.gov.pk, Zawar66@gmail.com*

offer several advantages compared to traditional electrode materials. Notably, MXenes exhibit high electrical conductivity, which facilitates rapid charge and discharge processes. Furthermore, their extensive surface area enhances charge storage capacity within the interlayer spaces. To date, extensive experimental evaluations have been conducted on various members of the MXene family. MXenes are defined by the chemical formula $M_{n+1}X_nT_x$ (where n ranges from 1 to 4), "M" represents a transition metal element (*e.g.*, Ti, V), "X" indicates carbon and/or nitrogen, and "T_x" denotes surface functional groups (*e.g.*, O^- H, O^-, with "x" varying). MXenes exhibit several advantageous properties for energy storage applications, including high theoretical capacities ($\approx$448 mA h g^{-1}) for monolayered Ti_3LiC_2, high metallic conductivity ($\approx$25 000 S m^{-1}), high density of redox-active sites, excellent mechanical strength, and tunable hydrophilicity.[11–15] MXenes solutions can be used to create flexible films that function as electrodes without additional conductive additives or binders. The versatility of MXenes allows for the precise tuning of their chemical composition, crystal structure, and surface chemistry to meet specific application requirements. MXenes composites further enhance the potential of energy storage systems by improving performance characteristics. MXenes and their derivatives are highly promising for use in various roles, including anodes, cathodes, current collectors, conductive binders, and electrolyte additives in a range of super-capacitors and secondary batteries. A study investigated the effects of additive-mediated intercalation and surface modification of MXenes and explored their potential applications across diverse fields such as energy storage, environmental technology, biology, electronics, and optics.[16] More recently, another study reviewed the advancements, critical performance factors, challenges, and prospects of MXenes-based macroforms in non-Li batteries and super-capacitors.[17]

Density functional theory (DFT) calculations offer valuable insights into the structural properties of MXenes, enabling the study of their stability, surface models, interfacial properties, and metal doping mechanisms. For example, the interfacial properties of tungsten disulfide (WS_2) in contact with various MXenes (Ti_2C, V_2C, C_2C, Zr_2C, Hf_3C_2, and Ti_3C_2) were analyzed using first-principles calculations, revealing strong coupling between MXenes and WS_2, resulting in WS_2 metallization and the formation of ideal ohmic contacts in the vertical direction.[18] Quantum transport simulations further demonstrated that Zr_2C and Hf_3C_2 electrodes produced small Schottky barrier, suggesting their suitability for high-performance WS_2-based transistors. DFT was also used to develop a structural model for $Ti_3C_2T_x$ MXene, correlating surface configuration with *c*-axis values, advancing *in situ* measurements of MXene surface structures.[19] Mo substitution was investigated through DFT, showing that replacing Ti with Mo in MXenes enhances bonding and electronic coupling between O, C, and metal atoms, transforming metallic $Ti_3C_2O_2$ into semiconducting $Mo_2TiC_2O_2$, consistent with experimental findings. Spin–orbit coupling played a crucial role, splitting the degenerate d-band and leading to band inversion important for topological properties.[20] Simulations revealed that termination configuration affects structure, stability, and electronic properties in $W_{1.33}C$ MXenes.[21] DFT calculations also explored the nearly free electron states of MXenes, demonstrating that the overlap of these states influences band gap width, which varies with interlayer distance. An applied electric field can tune this behavior, transforming $Sc_2C(OH)_2$ from a semiconductor to a metal, making it promising for electronic switching applications.[22]

The optical and electronic properties of various bimetallic MXenes were investigated, predicting at least 26 bimetallic 2D carbides, with experimental verification of $Mo_2TiC_2T_x$ and $Mo_2Ti_2C_3T_x$ MXenes, showing distinct electro-chemical behavior.[23] Further, the geometric, electronic, and optical properties of M_2CO_2 and MoS_2 hetero-structures were analyzed, indicating potential applications in water splitting[24] and electronics due to enhanced light absorption and high carrier mobility.[25] Lastly, DFT studies on bimetallic MXenes like $Ti_2(1-x)V_2xCO_2$ revealed superior conductivity compared to individual components, positioning it as a viable alternative to indium tin oxide for transparent conductive applications.[26]

MXene materials are investigated through the controlled removal of aluminum from layered MAX phases, resulting in carbide films that are subsequently exfoliated into two-dimensional MXene sheets, each comprising only a few atomic layers in thickness. These MXene sheets possess the capacity to intercalate various ions and molecules, a process that significantly enhances their distinctive properties. Notably, the intercalation of lithium ions between MXene sheets has been demonstrated to render them suitable for applications in electro-chemical capacitors and lithium-ion batteries. Fig. 1 illustrates the process how MXenes derived from the MAX phase.[27] The general formula for MXenes is $M_{n+1}X_nT_x$, where "M" represents a transition metal such as scandium, titanium, zirconium, or niobium, "X" signifies either nitrogen or carbon, and "T_x" refers to the surface terminations that are introduced during the synthesis process and consist of hydroxyl, fluorine, and oxygen.[28]

The $M_{n+1}X_nT_x$ phase is a fundamental formula for MXenes, generated through the selective etching of the A layers. This

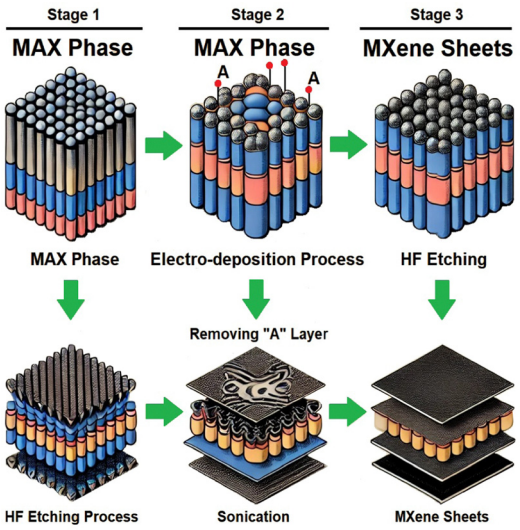

Fig. 1 Schematic of how MXenes are made from MAX phases.

etching process occurs because the M–A bonds and interatomic A–A bonds exhibit comparatively weaker metallic characteristics than the M–X bonds, which display ionic, metallic, or covalent attributes. The term T_x refers to surface terminations, such as fluorine (F^-), hydroxyl (O^- H), and oxygen (O^-), which adhere to the surfaces of the metal (M) atoms.[29] Polysulfides can interact with these polar functional groups located on the atomic surface, including metal sites and terminal functional groups, thereby effectively hindering unwanted reactions.

MXenes can be distinguished from other two-dimensional materials, such as graphene, due to their unique properties. The composition, morphology, surface functionalities, and crystal structure of MXenes can be tailored to enhance their intrinsic structural characteristics and performance across diverse applications. Exhibiting metallic-like behavior, MXenes demonstrate high electrical conductivity. The mechanical, chemical, and physical properties of MXenes are significantly influenced by the number of metal atomic layers, as evidenced by theoretical and computational studies. The superior physical and chemical properties of these two-dimensional (2D) materials, when compared to their bulk counterparts, have attracted considerable interest in various fields.[30,31]

The study in ref. 32 employs density functional theory (DFT) to thoroughly analyze the impact of MXene composition, surface structure, and lithium concentration on the reaction mechanisms in Li-ion energy storage systems. The results are pivotal in categorizing MXenes into two primary groups based on structural responses during lithium adsorption. Specifically, MXenes exhibit either a V-type structure, including compounds such as Ta_2CO_2 (tantalum carbide oxide) and Cr_2C_2 (chromium carbide), or a Sc-type structure, represented by Sc_2CO_2 (scandium carbide oxide), Hf_2CO_2 (hafnium carbide oxide), Nb_2CO_2 (niobium carbide oxide), Zr_2CO_2 (zirconium carbide oxide), and Ti_2CO_2 (titanium carbide oxide). Each group demonstrates distinct atomic rearrangements under lithium adsorption. The findings are crucial for advancing the understanding of how different MXene structures respond to lithium ion intercalation, which is essential for optimizing their performance in energy storage applications.

In electrical double-layer capacitors (EDLCs), charge storage occurs at the electrolyte interface, forming an electrostatic double layer. This mechanism is non-faradaic, meaning it does not involve redox reactions or electron transfer. Energy is stored in EDLCs purely through electrostatic interactions with the material. Conversely, pseudo-capacitors employ faradaic redox reactions or electron transfer processes, which are not significantly influenced by the electrode surface area. In pseudo-capacitors, electrolyte ions migrate through the electrode to reach a conductive bulk phase, even after redox reactions have transpired and the exchange of electrons or ions has taken place. Unlike in EDLCs, where charges remain within the electrode, pseudo-capacitors involve more dynamic charge transfer processes.

One of the primary challenges in MXene research is the development of scalable, safe, efficient, and environmentally friendly synthesis methods. Additional challenges include improving the chemical and thermal stability of MXenes and gaining a comprehensive understanding of their quantum confinement effects, as well as their electrical, optical, magnetic, thermal, and thermo-electric properties. To address these issues, researchers are designing 3D nano-architectures using vertically aligned, hybrid, and other configurations derived from 2D MXene materials in blocks.

In addition, it is crucial to comprehend how MXenes store charge in both non-aqueous and aqueous electrolytes for electro-chemical energy storage applications. Equally important is the ability of MXenes to impart their outstanding mechanical properties to composite materials consisting of ceramics and metals. Key considerations include the control of material properties through engineered defects, the investigation of physical characteristics (such as superconductivity), and the evaluation of health and environmental safety. Further research should focus on the discovery of new MXene compounds, the development of delamination techniques for MXenes beyond Ti_3XC_2, and methods that do not rely on organic intercalants.

Improvements in MXene aim to eliminate the reliance on aluminum MAX phases. This can be achieved through physical vapor deposition or chemical vapor deposition under vacuum conditions. Additionally, optimizing interface charge transfer mechanisms is essential. It is also critical to advance the development of 2D transition metal carbide Ti_3XC_2 to produce semiconducting MXenes with tailored band gaps.

Exploration of new precursors beyond MAX phases is necessary, alongside evaluating how precursor structure, defects, and stoichiometry affect MXene properties. There is also a need to develop MXenes that do not rely on titanium and to standardize characterization processes. A significant challenge in MXene research is the limited cation intercalation and high ionic diffusion resistance associated with single-layer stacking, which impairs electro-chemical performance. Enhancing electrical conductivity, stability, and ion/electron transport in MXene-based hybrid materials can be accomplished by optimizing the material architecture and increasing inter-layer spacing. This structural modification facilitates rapid ion and electrolyte diffusion, thereby significantly improving the electro-chemical performance of the materials.

2 Methodology

In this study, we utilized the full potential linear augmented plane wave (FP-LAPW) method, implemented through the WIEN2K computational code, which operates within the framework of density functional theory (DFT). This advanced computational technique allows for precise calculations of electronic structure and properties of materials at the atomic level. To ensure accurate results, we performed self-consistent iterations that converged to an energy tolerance of 0.0001 Ry (Rydberg), a measure of energy commonly used in quantum mechanics and solid-state physics. This stringent convergence criterion guarantees that the calculated electronic states reflect a stable solution of the underlying quantum mechanical equations. The fundamental crystal structures were meticulously

optimized to facilitate the determination of the density of states (DOS), which characterizes the number of electronic states available for occupation at each energy level. This optimization process involved following key steps:

1. Relaxation of atomic positions: atomic positions were optimized by minimizing inter-atomic forces, ensuring that the equilibrium configuration was achieved, thereby accurately representing the material's ground state.

2. Volume optimization: the volume of the crystal structure was optimized while maintaining a constant $a:c$ ratio (where 'a' and 'c' represent the lattice parameters). This approach ensures that the geometric proportions of the crystal are preserved during the optimization process.

3. Adjustment of cell parameters: the optimization included adjusting the cell parameters while keeping the overall volume constant. This technique helps in fine-tuning the lattice structure to achieve a more energetically favorable configuration.

For the initial structures of Ti_3XC_2, we referred to existing literature that provided foundational data on Ti_3AlC_2.[33,34] The space group for these structures was identified as $P63/mmc$, which is characteristic of certain layered materials and plays a crucial role in determining the symmetry properties of the crystal. To compute the Brillouin zone integrals, a k-point mesh of $15 \times 15 \times 15$ was employed using the monkhorst pack (MP) scheme. This approach enables the sampling of the reciprocal space, essential for accurately calculating electronic properties. Additionally, our calculations were performed using a spin-polarized ferromagnetic (FM) model under the perdew burke ernzerhof (PBE) and generalized gradient approximation (GGA).[35] The inclusion of spin polarization accounts for the magnetic interactions within the material, providing a more comprehensive understanding of its electronic structure and magnetic properties.[36] The PBE–GGA framework is widely recognized for its balance between computational efficiency and accuracy in describing exchange–correlation effects in many-body systems. The meticulous optimization of structural parameters and the application of advanced computational techniques enable us to derive meaningful insights into the electronic properties of Ti_3XC_2 compounds, contributing to the broader understanding of their potential applications in materials science and nanotechnology.[37–39]

In the WIEN2K computational package, which is widely used for performing calculations in the framework of density functional theory (DFT), each atom within the crystal structure is assigned a specific muffin-tin radius, denoted as R_{MT}. This muffin-tin approximation facilitates separation of the atomic potential into distinct regions; within each non-overlapping muffin-tin sphere surrounding the atoms and the interstitial spaces between these spheres. The electronic structure calculations rely on solving the time-independent schrödinger equation in spherical coordinates, which is particularly well-suited for the regions defined by the muffin-tin spheres. In these atomic spheres, the wave functions are expanded in terms of spherical harmonics, accommodating the local atomic potentials. Meanwhile, in the interstitial regions, where the atomic spheres do not overlap, the calculations utilize a plane-wave basis set. This dual approach allows for an efficient treatment of the electronic states, as the muffin-tin approximation can effectively capture the localized behavior of electrons near the atoms, while plane waves are adept at describing the delocalized states in the intervening space.

To achieve a precise representation of the wave functions, the plane-wave cut-off parameter is established at $K_{max} \cdot R_{MT} = 7.0$. Here, R_{MT} refers to the smallest muffin-tin radius in the unit cell, and K_{max} is defined as the magnitude of the largest K-vector in the reciprocal space. This cut-off parameter ensures that the basis set is sufficiently complete, capturing the essential features of the electronic wave functions while balancing computational efficiency. Additionally, the Fourier-expanded charge density is truncated at $G_{max} = 12(Ry)^{1/2}$, where G represents the reciprocal lattice vectors. This truncation is critical for managing the computational load, as it limits the number of terms in the Fourier expansion while still providing an accurate description of the charge distribution within the material. For the wave function expansion inside the muffin-tin spheres, the maximum angular momentum l_{max} is set to 10. This parameter determines the highest angular momentum state included in the expansion, thus influencing the completeness and accuracy of the electronic wave functions derived from the schrödinger equation. A higher l_{max} value allows for a more detailed representation of the angular dependence of the wave functions, which is particularly important in systems with complex electronic structures or where localized d or f states are present.

In this study, we systematically examined two distinct types of intercalated structures, denoted as the first deintercalated structure and the second deintercalated structure. The structural composition of the titanium carbide MXene Ti_3XC_2 is depicted in Fig. 3. The first deintercalation stage involves the removal of intercalating atoms of germanium (Ge), lead (Pb), and bismuth (Bi) from the relaxed MAX phases of **Ti_3GeC_2**, **Ti_3PbC_2**, and **Ti_3BiC_2** respectively. This removal process yields the Ti_3XC_2 structure, where X represents the intercalating element. Following this step, the system undergoes a relaxation process, leading to the stabilization of the first deintercalated structure. In the subsequent intercalation stage, an atom X (such as Ge, Pb, or Bi) is introduced into the previously vacated site within the Ti_3XC_2 framework. This insertion is accompanied by another relaxation process to establish the new intercalated structure. The final stage, termed the second deintercalation stage, entails the removal of the intercalating element from the intercalated Ti_3XC_2 structure (for instance, **Ti_3GeC_2**, **Ti_3PbC_2**, or **Ti_3BiC_2**). The resultant Ti_3XC_2 structure is then subjected to a relaxation process, culminating in the formation of the second deintercalated structure.

A comprehensive analysis of these intercalated structures is provided in the Results section, specifically in Section 3.1, where the implications of these structural modifications on the material properties are discussed in detail. This investigation explores the intricate mechanisms underlying the intercalation and deintercalation processes within MXenes, contributing to a deeper understanding of their structural dynamics and potential applications in various fields.

3 Results and analysis

3.1 Structural properties

The calculated structure of Ti_3XC_2 is tetragonal crystal structure. The molecular dynamic (MD) calculation were calculated at 1000 K shows in Fig. 2. which is a stable structure. The structures obtained from the first and second deintercalation stages are referred to as the 1st and 2nd deintercalated structures. The structure resulting from the intercalation stage is considered the intercalated structure. Tables 1 and 2 present the structural properties of Ti_3XC_2 MXenes at the first and second deintercalation stages, respectively. The assessment of structural stability is based on changes in cell volume during the deintercalation process with a volume change of less than 10% indicative of stability.[34] Table 1 in which X elements are inserted (intercalated) to Ti_3XC_2. **Ti_3GeC_2**, **Ti_3PbC_2**, and **Ti_3BiC_2** demonstrate the highest stability during the first deintercalation stage, while other existing MXenese compounds shows lower stability. However, Table 2 presents a revised stability ranking for the second deintercalation stage in which these elements have been partially or completely removed. For Ti_3XC_2 energy storage, where X represents Ge, Pb, and Bi. Despite variations in stability rankings, the second deintercalation stage results indicate that all Ti_3XC_2 MXene energy storage maintain adequate structural stability.

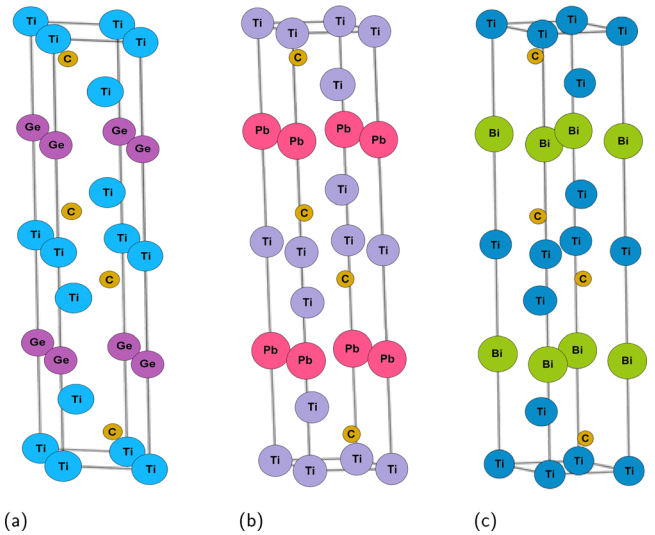

Fig. 2 Calculated structure of Ti_3XC_2 (X = Ge, Pb, or Bi) compounds: (a) **Ti_3GeC_2**, (b) **Ti_3PbC_2**, (c) **Ti_3BiC_2**.

For each material in Tables 1 and 2 includes three lattice parameters labeled as '*a*', '*b*', and '*c*', each measured in angstroms (Å), and the unit cell volume denoted as Omega (Ω) in cubic angstroms (Å^3). The structural changes that occur during the deintercalation process are highlighted by percentage differences in the lattice parameters and the overall unit cell volume. These percentage changes denoted as $\Delta x/x$ (%), quantify the structural expansion or contraction for each parameter and the total volume between the two states. Taking the material $Ti_1Li_2C_2$ as an example, the Table 1 shows that in its intercalated state, the lattice parameters are a = 3.08 Å, b = 3.08 Å, and c = 19.43 Å, resulting in a total unit cell volume of 570.6 Å^3. Upon deintercalation, the lattice parameters shift to a = 3.11 Å, b = 3.11 Å, and c = 18.04 Å, with the unit cell volume reducing to 540.8 Å^3. The corresponding percentage changes in the lattice parameters are $\Delta a/a$ = 1.01%, $\Delta b/b$ = 1.01%, $\Delta c/c$ = −7.11%, and the volume change $\Delta\Omega/\Omega$ is −5.22%. This trend of lattice parameter and volume variation upon deintercalation is consistently reported for each material in the Table 1, providing a comprehensive comparison of the

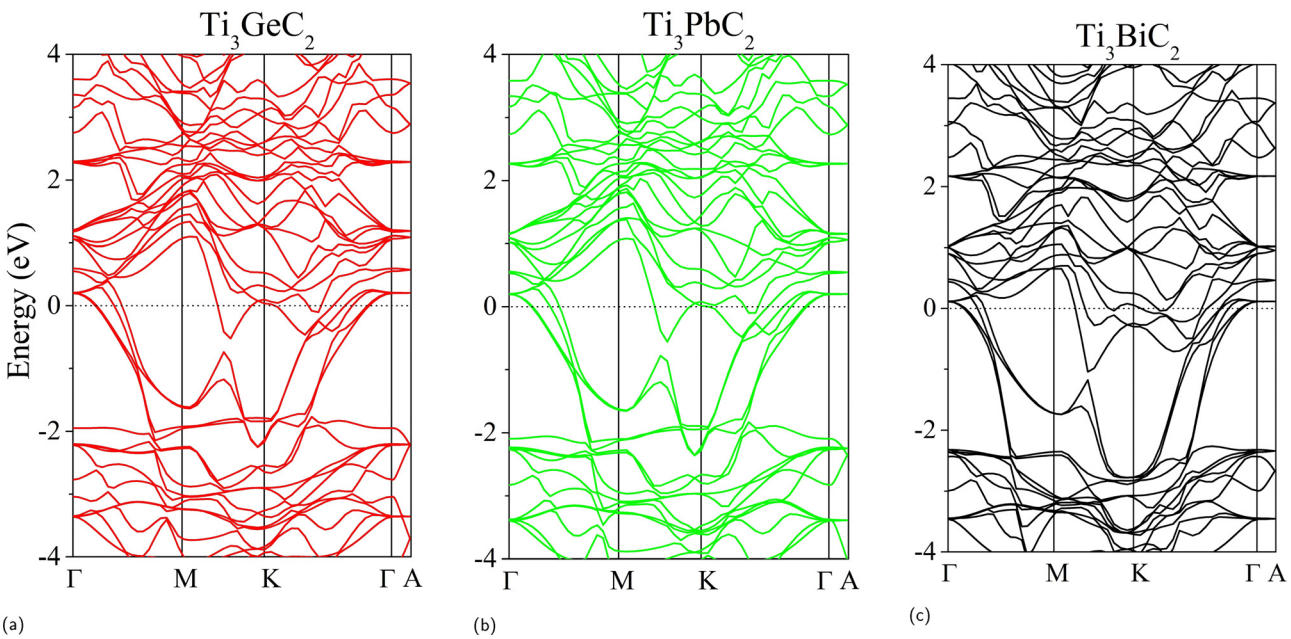

Fig. 3 Band structure (a) **Ti_3GeC_2** (b) **Ti_3PbC_2** (c) **Ti_3BiC_2**.

Table 1 Structural information for 1st deintercalation stage. calculated *via* GGA approximations for Ti_3XC_2 (X = Li,Na,Ca,Ge,Pb,Bi)[34]

Material	State	a (Å)	b (Å)	c (Å)	W (Å^3)
Ti_3LiC_2	Intercalated	3.08	3.08	19.43	570.6
	Deintercalated	3.11	3.11	18.04	540.8
	$\Delta x/x$(%)	1.01	1.01	−7.110	−5.22
Ti_3NaC_2	Intercalated	3.11	3.11	20.38	610.5
	Deintercalated	3.11	3.11	18.04	540.0
	$\Delta x/x$(%)	0.03	0.03	−11.45	−11.40
Ti_3CaC_2	Intercalated	3.16	3.16	20.92	647.5
	Deintercalated	3.11	3.11	18.05	540.8
	$\Delta x/x$(%)	−1.59	−1.59	−13.75	−16.50
Ti_3GeC_2	Intercalated	3.15	3.15	18.73	610.0
	Deintercalated	3.14	3.14	18.72	575.0
	$\Delta x/x$(%)	1.07	1.07	3.140	−5.39
Ti_3PbC_2	Intercalated	3.14	3.14	18.70	590.0
	Deintercalated	3.15	3.15	18.72	560.0
	$\Delta x/x$(%)	1.17	1.17	−1.290	−9.47
Ti_3BiC_2	Intercalated	3.21	3.21	18.72	620.0
	Deintercalated	3.19	3.19	18.73	590.0
	$\Delta x/x$(%)	0.97	0.97	1.170	−4.63

Table 2 Structural information for 2nd deintercalation stage. calculated *via* GGA approximations for Ti_3XC_2 (X = Li,Na,Ca,Ge,Pb,Bi)[34]

Material	State	a (Å)	b (Å)	c (Å)	W (Å^3)
Ti_3LiC_2	Intercalated	3.08	3.08	19.4	570.6
	Deintercalated	3.14	3.14	18.1	553.2
	$\Delta x/x$(%)	1.99	1.99	−6.82	−3.06
Ti_3NaC_2	Intercalated	3.11	3.11	20.4	610.5
	Deintercalated	3.13	3.13	19.5	589.4
	$\Delta x/x$(%)	0.50	0.50	−4.41	−3.45
Ti_3CaC_2	Intercalated	3.16	3.16	20.93	647.5
	Deintercalated	3.12	3.12	20.26	611.8
	$\Delta x/x$(%)	−1.21	−1.21	−3.12	−5.52
Ti_3GeC_2	Intercalated	3.01	3.41	17.7	581.0
	Deintercalated	3.19	3.56	18.2	570.0
	$\Delta x/x$(%)	1.39	1.41	1.50	−4.70
Ti_3PbC_2	Intercalated	3.09	3.19	3.20	611.0
	Deintercalated	3.87	3.69	3.23	597.0
	$\Delta x/x$(%)	1.09	1.12	1.20	−4.91
Ti_3BiC_2	Intercalated	3.29	3.19	3.07	527.0
	Deintercalated	3.92	4.10	4.12	501.0
	$\Delta x/x$(%)	0.96	0.90	0.82	−4.39

structural evolution during the intercalation and deintercalation processes. In Table 2, a similar pattern is observed as in Table 1, indicating improved stability with reduced volumetric changes.

Structural information between the first and second deintercalated states as presented in Tables 1 and 2, a clear consistency in the trend of lattice parameter changes can be observed across both states. For all materials listed (Ti_3LiC_2, Ti_3NaC_2, Ti_3CaC_2, **Ti_3GeC_2**, **Ti_3PbC_2**, and **Ti_3BiC_2**), there is a uniform decrease in the lattice parameters (a, b, c) upon deintercalation. This decrease is accompanied by a reduction in the volume (Å^3), signifying a contraction of the material structure in both deintercalated states. The percentage change in lattice parameters ($\Delta x/x$ %) remains relatively similar across both tables, further underscoring a consistent structural response in each case. Notably, materials such as Ti_3CaC_2, Ti_2GeC_2, **Ti_3PbC_2**, and **Ti_3BiC_2** exhibit significant changes in volume, indicating that these materials experience more pronounced structural contractions compared to Ti_3LiC_2 and Ti_3NaC_2, although the general trend remains consistent. The comparative analysis reveals that the deintercalation process leads to a predictable and uniform contraction in these materials, with no major deviations in behavior between the first and second deintercalated states.

The variations observed during the deintercalation stages are summarized in Table 3, and these changes have notable effects on both the electronic and structural properties of the material. These calculations are under GGA and GGA+U potential. As GGA+U approximation introduces a Hubbard U term to account for the on-set Coulomb interaction in localized d- or f-electrons system. This modification is particularly beneficial when transition metal atom like Ti is involved. GGA, GGA+U = 4, and GGA+U = 8 differ in their treatment of electron correlation effects, particularly for transition metal compounds, where d or f orbital electrons play a crucial role. The Hubbard correction term U better defines the electron–electron interactions. This adjustment often leads to more accurate predictions of electronic properties. For materials like Ti_3LiC_2, the observed variations in energy values between the internal and Fermi approaches across different deintercalation stages suggest notable shifts in the materials ability to release or intercalate ions. In the first deintercalation stage, the internal

Table 3 1st and 2nd deintercalation stages calculated *via* GGA and GGA+U (U = 4 and 8 eV) approximations for Ti_3XC_2 (X = Li,Na,Ca,Ge,Pb,Bi) by internal and Fermi energy approaches[35]

		1st deintercalation stage			2nd deintercalation stage		
Material	Approach	GGA	GGA+U = 4	GGA+U = 8	GGA	GGA+U = 4	GGA+U = 8
Ti_3LiC_2	Internal	0.72	0.71	0.66	0.84	1.03	1.19
	Fermi	0.32	0.37	0.42	0.08	0.02	0.04
Ti_3NaC_2	Internal	0.27	0.26	0.20	0.62	0.75	0.86
	Fermi	0.35	0.40	0.47	0.67	0.66	0.58
Ti_3CaC_2	Internal	0.31	0.06	0.49	0.68	0.09	0.50
	Fermi	2.19	2.22	2.29	1.05	1.05	1.09
Ti_3GeC_2	Internal	0.67	0.72	0.86	0.73	0.99	1.10
	Fermi	0.34	0.39	0.53	0.36	0.39	0.53
Ti_3PbC_2	Internal	0.72	0.82	0.91	0.62	0.72	0.69
	Fermi	0.09	0.30	0.52	1.02	0.99	0.86
Ti_3BiC_2	Internal	0.42	0.52	0.61	0.93	0.99	0.87
	Fermi	0.59	0.55	0.39	0.39	0.65	0.61

approach typically yields higher values compared to the Fermi approach, indicating stronger stability of the material during ion extraction under the internal method. As U increases the values slightly decrease for the internal approach, which implies that accounting for stronger electron correlation reduces the predicted binding energy of the deintercalated ions. In the second deintercalation stage, the increase in values for the internal approach, particularly as U increases, the material becomes more stable after partial ion extraction, suggesting a strengthened ionic framework post-deintercalation. However, the Fermi approach shows a drastic reduction in values in the second stage, indicating that under this approximation, the material exhibits weaker structural stability and reduced capability to hold onto intercalated ions. The broader impact of these shifts includes potential changes in the materials ion storage capacity, and conductivity. Higher stability in the second deintercalation stage, as observed in the internal approach indicate that the material could maintain structural integrity over longer cycles for energy storage devices. Conversely, the lower values in the Fermi approach suggest a higher tendency for material degradation or loss of performance over repeated cycles.

Intercalation and deintercalation are the reversible insertion and removal of guest species such as ions, atoms or molecules into or from the layered structure of Ti_3XC_2 compound without materially affecting their basic structural framework. These processes significantly influence the stability, electronic structure and other properties of studied compounds, making them for promising candidates for application in energy storage and optoelectronics.

The band structure diagrams (Fig. 3) for $\mathbf{Ti_3GeC_2}$, $\mathbf{Ti_3PbC_2}$, and $\mathbf{Ti_3BiC_2}$ reveals significant similarities and differences in their electronic properties and behaviors. The band structure of $\mathbf{Ti_3GeC_2}$, illustrated in Fig. 3a, displays energy levels spanning from −4 eV to 4 eV with high-symmetry points labeled, M, K, and A. The red curves indicate multiple electronic energy bands intersecting the horizontal dotted line at 0 eV, which signifies its metallic character. Notably, the presence of band crossings and degeneracies suggests intricate electronic interactions, while variations in band dispersion imply anisotropy in the material electronic structure. Similarly, Fig. 3b for $\mathbf{Ti_3PbC_2}$ shows an energy range of −4 eV to 4 eV with analogous high-symmetry points, where the green lines representing electronic bands exhibit various curves and crossings. The occurrence of multiple band crossings and avoided crossings indicating the complexity of electron interactions, vital for assessing the material conductive properties. In contrast, Fig. 3c for $\mathbf{Ti_3BiC_2}$ shares the same energy range and high-symmetry points but displays distinct characteristics. The curved lines reflect a variety of band behaviors with some steep slopes indicating high group velocities, while others are flatter. This band structure emphasizes complex quantum interactions and informs the understanding of $\mathbf{Ti_3BiC_2}$ electronic behavior, revealing potential conductive and optical characteristics.

3.2 Electronic properties

In Fig. 4, the charge density distributions in $\mathbf{Ti_3GeC_2}$, $\mathbf{Ti_3PbC_2}$, and $\mathbf{Ti_3BiC_2}$ provide valuable insights into their electronic

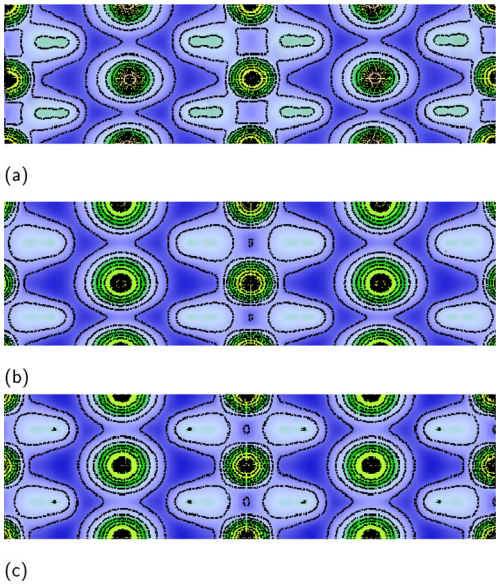

Fig. 4 Charge density (a) $\mathbf{Ti_3GeC_2}$ (b) $\mathbf{Ti_3PbC_2}$ (c) $\mathbf{Ti_3BiC_2}$.

structures and bonding characteristics, highlighting both similarities and differences across these compounds. In $\mathbf{Ti_3GeC_2}$ (Fig. 4a), the charge density is characterized by concentric circular patterns in green and yellow, indicative of regions with high charge density. The intensity of these colors signifies the magnitude of electron localization, with brighter areas representing higher charge densities. The blue-purple background contrasts with these high-density regions, denoting areas of lower electron concentration. The dashed white lines connecting the circular patterns suggest possible charge interactions and flow pathways, while light blue-green oval shapes may indicate regions of neutral charge or distinct charge variations. This structured nature of the charge distribution is likely reflective of its crystalline character. In $\mathbf{Ti_3PbC_2}$ (Fig. 4b), a similar symmetrical charge density distribution is observed, but with notable differences in intensity and bonding implications. The green regions, associated with higher charge densities, likely correspond to strong covalent Ti–C bonds, while the more diffuse areas related to Ti–Pb bonds suggest a metallic bonding character. This distribution is consistent with the layered structure of MAX phases, leading to anisotropic electronic properties. The grid-like formation enhances the analysis of charge behavior, emphasizing the relationship between charge density and bonding nature.

Charge density Fig. 4 show the spatial distribution of electrons surrounding atoms as well as the form of bonding. In $\mathbf{Ti_3GeC_2}$, strong charge localization between Ti and C atoms suggests considerable Ti-d and C-p orbital hybridization, which is typical of strong metallic bonding. Ge exhibits low charge accumulation, implying poorer Ti–Ge bonding than Ti–C. In $\mathbf{Ti_3PbC_2}$, Pb has a more confined charge distribution due to the inner pair effect, indicating poor bonding with Ti. The charge between Ti and C atoms remains significant, like $\mathbf{Ti_3GeC_2}$. Similarly, $\mathbf{Ti_3BiC_2}$Bi exhibits stronger charge localization, with

some asymmetry owing to relativistic spin–orbit coupling effects. The bonding strength between Ti and Bi is less than Ti–C. The conduction in **Ti_3GeC_2** exhibits steep curvature near the Fermi level indication lower effective mass and high carries mobility. In **Ti_3PbC_2**, Pb-p orbitals cause a moderate flattening of the conduction bands, resulting in slightly reduced mobility compared to Ti_2GeC_2. Similarly, the spin orbital coupling of **Ti_3BiC_2** due to Bi further flattens the conduction bands leading to more localized electrons states and reduced mobility.

The density of states (DOS) analyses for the materials **Ti_3GeC_2**, **Ti_3PbC_2**, and Ti_3Bi_2C provide critical insights into their electronic structures by illustrating the distribution of electronic states across various energy levels. Each graph spans an energy range from −4 eV to 4 eV on the *x*-axis, with the *y*-axis indicating the density of states in states per electron volt, reaching values up to 25 states per eV. The total DOS is represented by a black curve, which integrates contributions from distinct atomic orbitals across the constituent elements. Notably, while **Ti_3GeC_2** demonstrates a balanced distribution of contributions from Ti, Ge, and C orbitals (Fig. 5a), **Ti_3PbC_2** reveals pronounced peaks primarily from Ti-d states, indicating a significant role of titanium in defining its electronic behavior (Fig. 5b). In contrast, Ti_3Bi_2C shows distinct contributions from Bi orbitals, suggesting a potential variation in electronic characteristics relative to the other two materials (Fig. 5c).

In **Ti_3GeC_2**, the contributions from Ti-s, Ti-p, and Ti-d states highlight the complexity of the electronic structure, with Ge and C also playing integral roles. The analysis elucidates how these orbitals collectively impact the materials conductivity and potential applications in electronics (Fig. 5a). **Ti_3PbC_2** contrasts this, as the DOS reveals a marked dip near 0 eV, indicating the presence of a band gap or pseudo-gap, which could point to semiconducting or semi-metallic behavior (Fig. 5b). This behavior is reinforced by the dominance of Ti-d states in the positive energy range, suggesting enhanced electronic activity in this region. Meanwhile, Ti_3Bi_2C illustrates a more even distribution of states across its constituent orbitals, with notable contributions from Bi, emphasizing its role in modifying the electronic properties compared to the titanium carbide systems (Fig. 5c). The comparative DOS analysis of these materials underscores the differing roles of elemental orbitals in shaping their electronic properties. While **Ti_3GeC_2** and Ti_3Bi_2C present more uniform contributions across their atomic species, **Ti_3PbC_2** exhibits distinct peaks that suggest a unique electronic behavior influenced primarily by titanium. This information is vital for tailoring these materials for specific applications in electronic devices, enhancing performance by leveraging their unique electronic characteristics.

In Fig. 6a, the real part of the conductivity for the MAX-phase compounds **Ti_3GeC_2**, **Ti_3PbC_2**, and **Ti_3BiC_2** is depicted as a function of energy, with the *x*-axis representing energy in electron volts (eV) from 0 to 50 eV and the *y*-axis representing conductivity in units of inverse femto-seconds (1/fs) from 0 to 80. The results indicate that all three materials exhibit similar general trends while displaying unique characteristics. Notably, **Ti_3PbC_2** demonstrates the highest initial conductivity at low

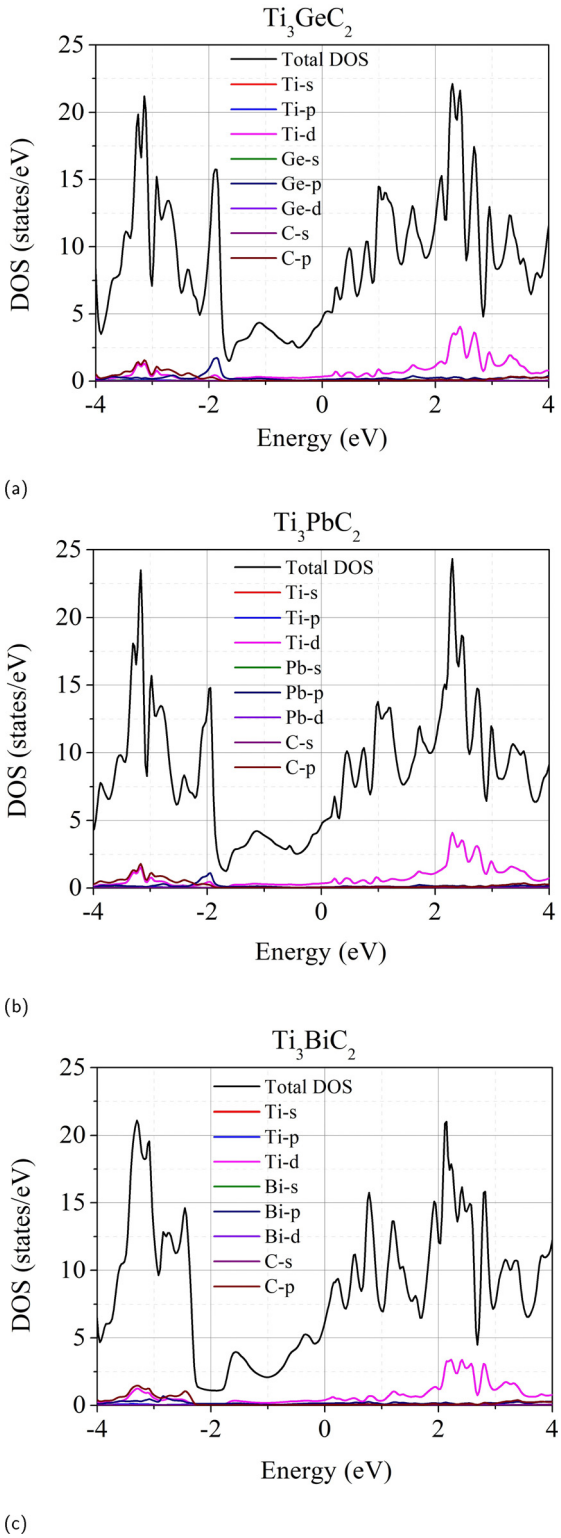

Fig. 5 DOS (a) **Ti_3GeC_2** (b) **Ti_3PbC_2** (c) **Ti_3BiC_2**.

energies, marked by a sharp peak near 0 eV, contrasting with the lower initial conductivity peaks observed for **Ti_3GeC_2** and **Ti_3BiC_2**. Fluctuations in conductivity are evident at energies below 10 eV, alongside a modest peak around 35–40 eV. Beyond these fluctuations, a general decrease in conductivity occurs,

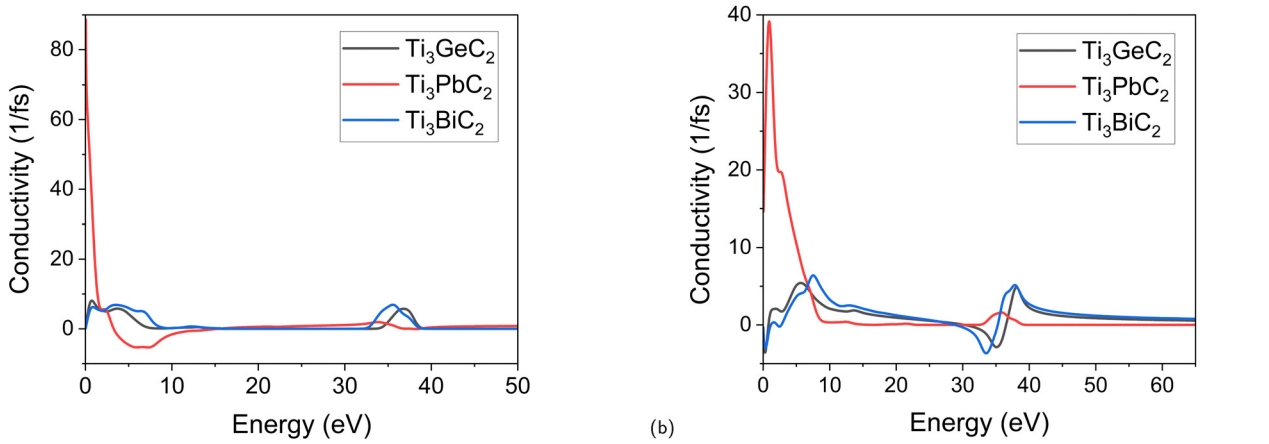

Fig. 6 Conductivity (a) real part (b) imaginary part.

stabilizing as energy increases. The conductivity values across most of the energy range remain between 0 and 10 1/fs, underscoring the distinctive behavior of Ti_3PbC_2 at low energies.

Fig. 6b illustrates the imaginary part of the conductivity for the same compounds, plotted against energy, where the energy axis ranges from 0 to 60 eV and the conductivity axis spans from 0 to 40 1/fs. In this context, Ti_3PbC_2 again reveals a prominent feature at low energies, exhibiting a peak approaching 40 1/fs. Conversely, Ti_3GeC_2 and Ti_3BiC_2 display lower peak values while maintaining similar overall trends. The conductivity variations across the energy spectrum are complex, with a notable dip around 35–40 eV followed by a minor peak. After 45 eV, all compounds exhibit stabilization at relatively low conductivity values.

The graph depicted in Fig. 7a illustrates the variation of the real part of dielectric function as a function of energy measured in electron volts (eV) for Ti_3GeC_2, Ti_3PbC_2, and Ti_3BiC_2. The energy values are plotted on the *x*-axis, spanning from 0 to 60 eV, while the dielectric function values are shown on the *y*-axis with a range extending from 0 to 400. Each compound is represented by a distinct line color, black for Ti_3GeC_2, red for Ti_3PbC_2, and blue for Ti_3BiC_2. The dielectric functions of all three materials exhibit a similar trend, characterized by initially high values at lower energy levels followed by a steep decline as the energy increases. By the time the energy approaches 60 eV, the dielectric functions of all three compounds converge toward very low values. Notably, the lines corresponding to these compounds remain closely aligned throughout the energy range implying that Ti_3GeC_2, Ti_3PbC_2, and Ti_3BiC_2 display nearly identical dielectric responses across the energy spectrum analyzed.

The graph labeled as Fig. 7b, depicts the imaginary part of the dielectric function plotted against energy, measured in electron volts (eV). The graph contains three distinct curves, each representing Ti_3GeC_2, Ti_3PbC_2, and Ti_3BiC_2, illustrated by black, red, and blue lines, respectively. Structurally, the graph has a vertical axis labeled "dielectric function," which spans from 0 to 140, and a horizontal axis labeled "energy (eV)," ranging from 0 to 50 eV. Each curve demonstrates a high initial

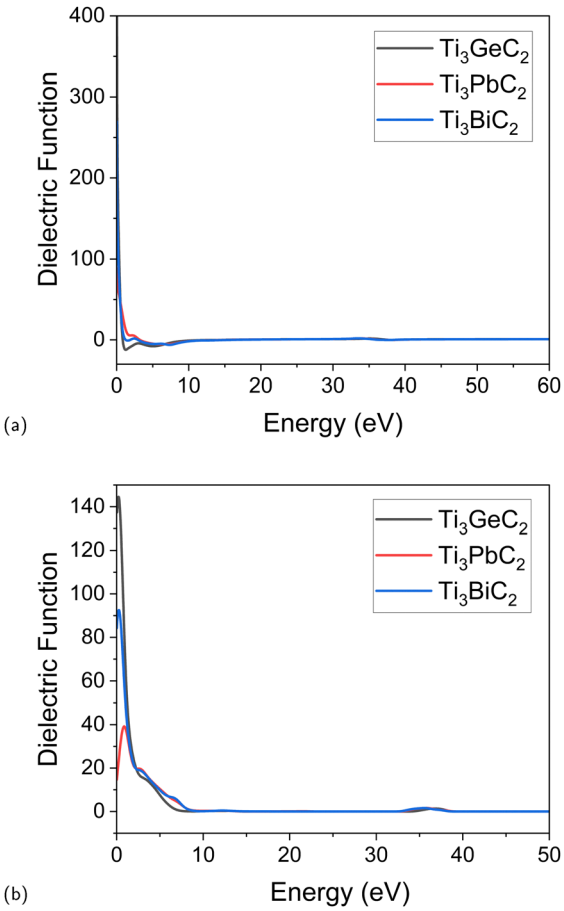

Fig. 7 Dielectric function (a) real part (b) imaginary part.

value at low energy, followed by a sharp decline as the energy increases, particularly noticeable within the range of 0 to 10 eV. Fig. 7a and b show maximum value near to 2 eV for both real and imaginary part. At 2 eV, a significant interband transition occurs in the material. This correspondence to electrons being excited from occupied electronic states (valence band) to unoccupied states (conduction band). These transitions contribute

strongly to the imaginary part of the dielectric function. Through the Kramers–Krong relation peak in imaginary part influence the dispersion, leading to a maximum in real part at corresponding energy. A maximum value in the real part often indicates that the materials exhibit strong polarization effect near the 2 eV. This result show that there are strong electronic polarization due to the density of states near the Fermi level. The maximum value in real part near 2 eV indicates efficient energy storage in the materials making it high polarizable under an external electric field.

Among the three materials, **Ti_3GeC_2** exhibits the highest starting value, while **Ti_3PbC_2** follows, and **Ti_3BiC_2** shows the lowest initial value. After the steep initial drop, all curves begin to stabilize and display minor oscillations but generally remain flat at higher energy levels. The rapid decrease in dielectric function values at lower energies suggests a significant energy dependence within this range. As energy increases, the curves converge, indicating that the dielectric properties of the three materials become more similar at higher energy levels.

3.3 Optical properties

The optical properties of MXenes are characterized by their interaction with light or electromagnetic radiation across a broad wavelength spectrum ranging from the infrared (760–780 nm to 1 mm) to ultraviolet (100–400 nm). Among the diverse optical properties of MXenes, key aspects include electrochemiluminescence, light absorption, and photoluminescence. These properties are extensively utilized in various fields such as optoelectronic devices, biomedical applications, and photocatalysis. MXenes exhibit exceptional photothermal conversion efficiency due to their superior optical characteristics, which can be further enhanced by surface modifications.

Optical absorption in the infrared or ultraviolet spectrum is essential for applications in photovoltaic, photocatalytic, transparent, and optically conductive electrodes. Ti_3XC_2 films are capable of absorbing light within the 300–500 nm wavelength range in the UV-visible spectrum. Absorption in this range is associated with electronic transitions that fall within the material's visible energy band structure. It determines a material's color, which displays technology in solar cells, and pigment characterization. The electron density significantly influences plasmonic absorption, which can be tuned by altering the X components of the MXene and modifying its electronic structure. For instance, **Ti_3BiC_2** (Fig. 5c) with a smaller density of states (DOS) of 21.2 states per eV at the Fermi level exhibits a lower and blue-shifted plasmonic peak compared to **Ti_3GeC_2** with 22.1 states per eV (Fig. 5a) and **Ti_3PbC_2** with 24.7 states per eV (Fig. 5b). Density functional theory (DFT) studies suggest that the highest DOS of 24.7 states per eV in **Ti_3PbC_2** increases light absorption (Fig. 5c).

The absorption of **Ti_3PbC_2** and **Ti_3BiC_2** is observed to be higher compared to **Ti_3GeC_2** (Fig. 8a). The absorption *versus* energy graph for **Ti_3GeC_2**, **Ti_3PbC_2**, and **Ti_3BiC_2** materials provides insight into how absorption properties vary with energy levels across these materials. The energy distribution has a mean of 5.0 eV with a standard deviation of 2.93,

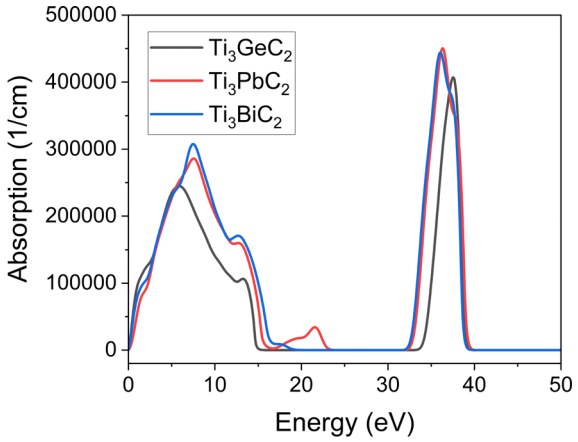

(a) Absorption

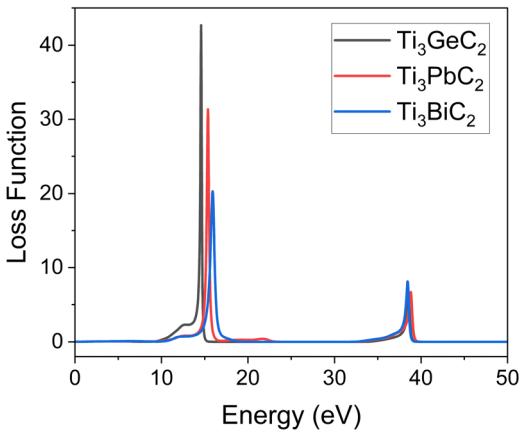

(b) Loss function

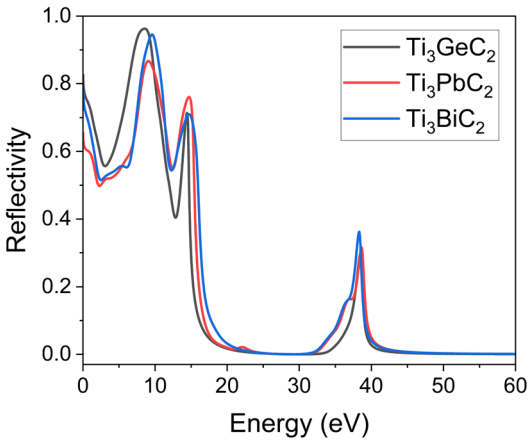

(c) Reflectivity

Fig. 8 Energy verses absorption, loss function, and reflectivity.

indicating a broad and uniform spread across the energy range. For **Ti_3GeC_2**, the absorption profile has a mean value of approximately 5.06 with a standard deviation of 1.01, showing a slight positive skewness. This suggests that most absorption

values are clustered just below and around the mean with a gradual increase toward higher absorption values. In the case of Ti_3PbC_2, the absorption mean is around 6.10 with a standard deviation of 1.25, also exhibiting slight positive skewness. This indicates that absorption values for Ti_3PbC_2 tend to accumulate just below and near the mean with a tail extending toward higher absorption levels. Ti_3BiC_2, on the other hand has a mean absorption of approximately 6.91 with a standard deviation of 1.44. The distribution of absorption values here is nearly normal with most values tightly grouped around the mean, showing less deviation compared to the other materials. The correlations between energy and absorption for all three materials, implying that energy variations have a minimal direct effect on absorption characteristics. This dependence suggests that absorption behavior in these materials is governed by factors other than energy, and the changes in energy levels across the range studied do not significantly influence absorption.

Loss function in Fig. 8b depicts the loss function as a function of energy (eV) for Ti_3GeC_2, Ti_3PbC_2, and Ti_3BiC_2. The *x*-axis represents the energy range from 0 to 50 eV, while the *y*-axis shows the loss function, with values reaching up to approximately 45. The loss function indicates the extent to which electrons interacting with the material lose energy, likely derived from electron energy loss spectroscopy (EELS). The most noticeable feature in the graph is the presence of two significant peaks for each compound. The first, a sharp and prominent peak occurs around 15–16 eV. This suggests a strong interaction between the high-energy electrons and the material corresponding to plasmon resonance, which refers to collective oscillations of the electron cloud at specific energy levels. The second, smaller peak appears between 38 and 40 eV, which correspond to higher-order electronic transitions or less intense resonant interactions within the material structure. Among the three compounds, Ti_3GeC_2 exhibits the highest peak with a loss function value exceeding 40. This indicates that the interaction between the electrons and Ti_3GeC_2 at around 15–16 eV is stronger compared to Ti_3PbC_2 and Ti_3BiC_2, which display similar but slightly lower peak intensities. This difference suggests a variation in the electronic structure or plasmonic behavior of Ti_3GeC_2 relative to the other two compounds. Between the two peaks, as well as beyond the second peak, the loss function for all three compounds drops close to zero indicating minimal energy loss and implying that no significant electron interactions occur within these energy ranges. Lower optical losses increase the amount of light absorbed by the active layer, maximizing energy conversion efficiency, which may be used in thin film solar cells and perovskite solar cell.

The graph in Fig. 8c illustrates the reflectivity of Ti_3GeC_2, Ti_3PbC_2, and Ti_3BiC_2 plotted as a function of energy, and measured in electron volts (eV). The *x*-axis represents energy, while the *y*-axis shows reflectivity, a dimensionless value ranging from 0 to 1. All three materials exhibit similar behavior with reflectivity rising to prominent peaks around 15 eV and 40 eV. Beyond the 40 eV peak reflectivity of all materials declines sharply, indicating a decrease in their ability to reflect energy at higher levels. The similarities in the reflectivity trends of these materials suggest that they share comparable optical properties, despite their different chemical compositions.

The figure referenced as Fig. 9a, represents the real part of the reflective index for Ti_3GeC_2, Ti_3PbC_2, and Ti_3BiC_2 as a function of energy. The *x*-axis of the graph spans from 0 to 60 eV, while the *y*-axis, labeled "reflective index," ranges from 0 to 20. All three materials show a rapid decrease in reflective index at lower energy levels (0–5 eV) followed by a relatively stable response at higher energy levels. Ti_3BiC_2 initially presents the highest reflective index at 0 eV. Between 5 and 40 eV, the differences in reflective index between the materials are minimal with all curves showing small fluctuations, including peaks and dips between 30 and 40 eV. Beyond 40 eV, the curves converge.

Fig. 9b illustrates the behavior of the imaginary part of the reflective index as a function of photon energy measured in electron volts. The graph demonstrates that at 0 eV, all three materials exhibit high reflective indices, which rapidly decline as energy increases up to approximately 10 eV. Among the materials, Ti_3GeC_2, represented by the black line, consistently shows the highest reflective index over the entire energy range.

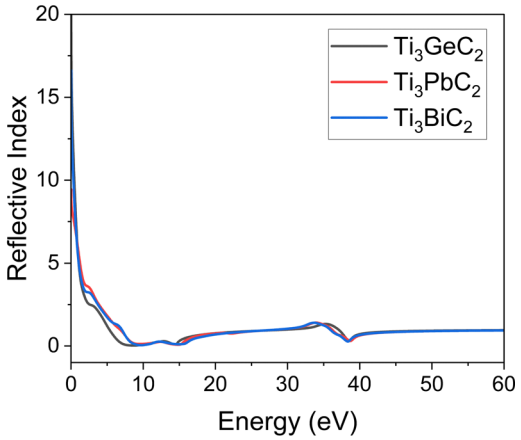

(a)

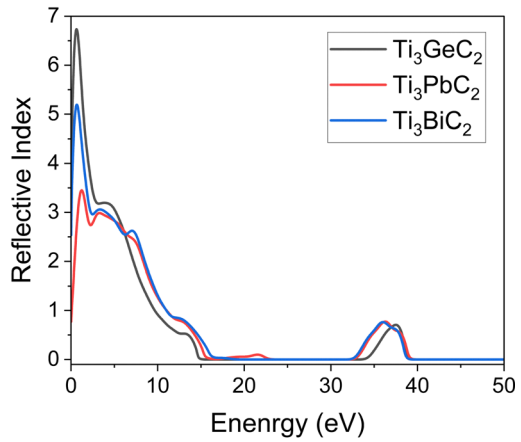

(b)

Fig. 9 Reflective index (a) real part (b) imaginary part.

This is followed by Ti_3PbC_2 (red line), and Ti_3BiC_2 (blue line), which both exhibit lower values. A distinct feature in the graph is a noticeable peak in the reflective index around 30 eV, where Ti_3BiC_2 shows a slightly higher maximum compared to the other two materials. After this peak, the reflective index of all materials decreases once again.

4 Conclusions

This study provides a detailed investigation of the structural, electronic, and optical properties of Ti_3XC_2 MXenes, focusing on their potential as energy storage materials for intercalation energy storage devices utilizing Ge, Pb, and Bi ions. Our findings highlight the initial instability encountered during the first stage of deintercalation, which emphasizes the importance of the enhanced structural stability observed in the second deintercalation stage. This stability is critical for the effective operation of energy storage devices.

The analysis revealed that Ti_3XC_2 MXenes exhibit metallic behavior characterized by a zero band gap, affirming their suitability for various electronic applications. The introduction of intercalated ions notably improves the electronic properties, making these materials promising candidates for efficient energy storage devices. Additionally, the optical properties exhibited by Ti_3PbC_2 indicate significant potential for applications in optoelectronic devices and photocatalysis.

These findings advance the understanding of Ge, Pb, and Si based MXenes as energy storage materials and establish a solid foundation for future research aimed at optimizing their performance. By elucidating the effects of intercalation on structural and electronic characteristics, new opportunities are created for exploring tailored modifications and practical applications in next-generation energy storage technologies.

Author contributions

Haider Hussain: conceptualization, methodology, software, validation, formal analysis, investigation, data curation, writing – original draft preparation. Zulfiqar Ali Shah: conceptualization, methodology, supervision, project administration. Syed Zafar Ilyas: supervision, writing – review, project administration. Abdul Shakoor: software resources, conceptualization, writing – draft preparation, editing & visualization. Zawar Hussain: review, writing – draft preparation & editing.

Data availability

All data supporting the findings of this study are contained within the article. Any additional datasets generated or analyzed during the study are available from the corresponding author on request.

Conflicts of interest

There are no conflicts to declare.

Notes and references

1 P. Li, G. Zhao, X. Zheng, X. Xu, C. Yao, W. Sun and S. X. Dou, *Energy Storage Mater.*, 2018, **15**, 422–446.
2 Y. An, Y. Tian, H. Shen, Q. Man, S. Xiong and J. Feng, *Energy Environ. Sci.*, 2023, **6**, 4191–4250.
3 X. Yang, Y. Yao, Q. Wang, K. Zhu, K. Ye, G. Wang, D. Cao and J. Yan, *Adv. Funct. Mater.*, 2022, **32**, 2109479.
4 K. Ren, Y. Yan, Z. Zhang, M. Sun and U. Schwingenschlögl, *Appl. Surf. Sci.*, 2022, **604**, 154317.
5 H. Luo, H. Liu, H. Huang, Y. Song, M. G. Tucker, Z. Sun, Y. Yao, B. Gao, Y. Ren, M. Tang, H. Qi, S. Deng, S. Zhang and J. Chen, *Sci. Adv.*, 2023, **9**, eade7078.
6 Z. Zhao, S. Wang, F. Wan, Z. Tie and Z. Niu, *Adv. Funct. Mater.*, 2021, **31**, 2101302.
7 W. Bi, J. Wang, E. P. Jahrman, G. T. Seidler, G. Gao, G. Wu and G. Cao, *Small*, 2019, **15**, e1901747.
8 Y. Yue and H. Liang, *Adv. Energy Mater.*, 2017, **7**, 1602545.
9 X. Wang, L. Meng, B. Li and Y. Gong, *Mater. Today*, 2021, **47**, 108–130.
10 C. Zhong, M. Sun, T. Altalhi and B. I. Yakobson, *Materials*, 2024, **17**, 1967.
11 T. S. Mathis, K. Maleski, A. Goad, A. Sarycheva, M. Anayee, A. C. Foucher, K. Hantanasirisakul, C. E. Shuck, E. A. Stach and Y. Gogotsi, *ACS Nano*, 2021, **15**, 6420–6429.
12 F. Wu, Y. Jiang, Z. Ye, Y. Huang, Z. Wang, S. Li, Y. Mei, M. Xie, L. Li and R. Chen, *J. Mater. Chem. A*, 2019, **7**, 1315–1322.
13 J. Gonzalez-Julian, *J. Am. Ceram. Soc.*, 2021, **104**, 659–690.
14 M. Greaves, S. Barg and M. A. Bissett, *Batteries Supercaps*, 2020, **3**, 211.
15 Q. Zhang, R. Fan, W. Cheng, P. Ji, J. Sheng, Q. Liao, H. Lai, X. Fu, C. Zhang and H. Li, *Adv. Sci.*, 2022, **9**, 2202748.
16 C. Li, J. Guo, C. Wang, D. Ma and B. Wang, *Appl. Surf. Sci.*, 2020, **527**, 146701.
17 F. Li, Y. Anjarsari, J. Wang, R. Azzahiidah, J. Jiang, J. Zou, K. Xiang, H. Ma and Arramel, *Carbon Lett.*, 2023, **33**, 1321–1331.
18 W. Tang, M. Sun, Q. Ren, S. Wang and J. Yu, *Appl. Surf. Sci.*, 2016, **376**, 286–289.
19 J. Wen, X. Zhang and H. Gao, *Phys. B*, 2018, **537**, 155–161.
20 L. Li, *Comput. Mater. Sci.*, 2016, **124**, 8–14.
21 R. Meshkian, H. Lind, J. Halim, A. El Ghazaly, J. Thörnberg, Q. Tao, M. Dahlqvist, J. Palisaitis, P. O. Ã. Persson and J. Rosen, *ACS Appl. Nano Mater.*, 2019, **2**, 6209–6219.
22 J. Zhou, M. Khazaei, A. Ranjbar, V. Wang, T. D. Kühne, K. Ohno, Y. Kawazoe and Y. Liang, *J. Mater. Chem. C*, 2020, **8**, 5211–5221.
23 Y. Luo, Y. He, Y. Ding, L. Zuo, C. Zhong, Y. Ma and M. Sun, *Inorg. Chem.*, 2024, **63**, 1136–1141.
24 B. Anasori, C. Shi, E. J. Moon, Y. Xie, C. A. Voigt, P. R. C. Kent, S. J. May, S. J. L. Billinge, M. W. Barsoum and Y. Gogotsi, *Nanoscale Horiz.*, 2016, **1**, 227–234.
25 X. Xu, X. Ge, X. Liu, L. Li, K. Fu, Y. Dong, F. Meng, R. Si and M. Zhang, *Ceram. Int.*, 2020, **46**, 13377–13384.

26 M. Naguib, O. Mashtalir, J. Carle, V. Presser, J. Lu, L. Hultman, Y. Gogotsi and M. W. Barsoum, *ACS Nano*, 2012, **6**, 1322–1331.
27 R. M. Ronchi, J. T. Arantes and S. F. Santos, *Ceram. Int.*, 2019, **45**, 18167–18188.
28 V. M. Hong Ng, H. Huang, K. Zhou, P. S. Lee, W. Que, J. Z. Xu and L. B. Kong, *J. Mater. Chem. A*, 2017, **5**, 3039–3068.
29 B. Li, P. Gu, Y. Feng, G. Zhang, K. Huang, H. Xue and H. Pang, *Adv. Funct. Mater.*, 2017, **27**, 1605784.
30 X. Guo, S. Zheng, G. Zhang, X. Xiao, X. Li, Y. Xu, H. Xue and H. Pang, *Energy Storage Mater.*, 2017, **9**, 150–169.
31 S. Wu, Y. Du and S. Sun, *Chem. Eng. J.*, 2017, **307**, 189–207.
32 G. Zhang, X. Xiao, B. Li, P. Gu, H. Xue and H. Pang, *J. Mater. Chem. A*, 2017, **5**, 8155–8186.
33 H. Liu, C. Duan, C. Yang, X. Chen, W. Shen and Z. Zhu, *Mater. Sci. Eng., C*, 2015, **53**, 43–49.
34 A. Ray, A. Roy, M. Ghosh, J. Alberto Ramos-Ramon, S. Saha, U. Pal, S. K. Bhattacharya and S. Das, *Appl. Surf. Sci.*, 2019, **463**, 513–525.
35 R. Li, L. Zhang, L. Shi and P. Wang, *ACS Nano*, 2017, **11**, 3752–3759.
36 A. R. Selvaraj, D. Chinnadurai, I. Cho, J.-S. Bak and K. Prabakar, *J. Energy Storage*, 2022, **52**, 104928.
37 H. Shu and X. Liu, *J. Mater. Chem. C*, 2023, **11**, 15074–15083.
38 K. Ren, H. Shu, W. Huo, Z. Cui, J. Yu and Y. Xu, *Phys. Chem. Chem. Phys.*, 2021, **23**, 24915–24921.
39 H. Shu, Y. Wang and M. Sun, *Phys. Chem. Chem. Phys.*, 2019, **21**, 15760–15766.